Formin homology 2 domain–containing 3 (Fhod3) controls neural plate morphogenesis in mouse cranial neurulation by regulating multidirectional apical constriction

Received for publication, August 21, 2018, and in revised form, December 19, 2018 Published, Papers in Press, December 20, 2018, DOI 10.1074/jbc.RA118.005471

Hikmawan Wahyu Sulistomo[‡], **Takayuki Nemoto**[‡], **Toshihiko Yanagita**[§], **and Ryu Takeya**[‡,1]

From the [‡]*Department of Pharmacology, Faculty of Medicine, University of Miyazaki, Miyazaki 889-1692, Japan and the* [§]*Department of Clinical Pharmacology, School of Nursing, Faculty of Medicine, University of Miyazaki, Miyazaki 889-1692, Japan*

Edited by Velia M. Fowler

Neural tube closure requires apical constriction during which contraction of the apical F-actin network forces the cell into a wedged shape, facilitating the folding of the neural plate into a tube. However, how F-actin assembly at the apical surface is regulated in mammalian neurulation remains largely unknown. We report here that formin homology 2 domain–containing 3 (Fhod3), a formin protein that mediates F-actin assembly, is essential for cranial neural tube closure in mouse embryos. We found that Fhod3 is expressed in the lateral neural plate but not in the floor region of the closing neural plate at the hindbrain. Consistently, in Fhod3-null embryos, neural plate bending at the midline occurred normally, but lateral plates seemed floppy and failed to flex dorsomedially. Because the apical accumulation of F-actin and constriction were impaired specifically at the lateral plates in Fhod3-null embryos, we concluded that Fhod3-mediated actin assembly contributes to lateral plate–specific apical constriction to advance closure. Intriguingly, Fhod3 expression at the hindbrain was restricted to neuromeric segments called rhombomeres. The rhombomere-specific accumulation of apical F-actin induced by the rhombomere-restricted expression of Fhod3 was responsible for the outward bulging of rhombomeres involving apical constriction along the anteroposterior axis, as rhombomeric bulging was less prominent in Fhod3-null embryos than in the wild type. Fhod3 thus plays a crucial role in the morphological changes associated with neural tube closure at the hindbrain by mediating apical constriction not only in the mediolateral but also in the anteroposterior direction, thereby contributing to tube closure and rhombomere segmentation, respectively.

Neurulation involves three-dimensional changes in the shape of the neural plate, where neuroepithelial cells tightly interconnected as a sheet undergo dynamic cell shape changes and reorganization of cell–cell junctions (1, 2). These morphological processes of neuroepithelial cells are controlled spatially and temporally by rearrangement of the cytoskeleton, including the apical junctional complex lined with F-actin (3, 4). Contraction of the F-actin network in the apical junctional complex causes apical constriction of individual neuroepithelial cells, leading to the localized bending and invagination of the neural plate. The assembly of F-actin at the apical junctional complex is regulated by multiple mechanisms, including Rho-family small GTPases and their effectors (5–7). The Arp2/3 complex, an actin nucleator activated downstream of Rac1 or Cdc42 signaling to create branched F-actin, has been shown to play important roles in the formation of F-actin at apical junctions (8–12).

Formins, another group of actin nucleators that promote the formation of linear unbranched F-actin downstream of RhoA signaling (13–16), also seem to participate in junctional actin polymerization (7, 17). In *Drosophila*, the formin-family protein Diaphanous regulates F-actin assembly at apical junctions of epithelial cells to direct diverse morphogenetic processes, *i.e.* dorsal closure, germband retraction (18), and formation of epithelial tubes including the tracheae, salivary glands, and hindgut (19). In zebrafish, the formin Fmnl3 is required for vessel lumen formation during embryogenesis (20). In contrast, in mammals, the roles of formins in the epithelium have been investigated mainly by using *in vitro* model systems, *i.e.* monolayer cells cultured on two-dimensional dishes or spheroid culture models in three-dimensional matrices (21–25), which mimic but are still different from *in vivo* morphogenetic processes. Thus, the *in vivo* role of mammalian formins in epithelial morphogenesis during embryonic development remains unclear.

We have shown previously that Fhod3, a formin-family protein that is expressed abundantly in the heart and to a lesser extent in the brain and kidney, plays an essential role in cardiogenesis by organizing cardiac myofibrillogenesis (26). In that study, Fhod3-null embryos died around E11.5 because of defects in cardiac development but also showed defects in neural tube closure, and the transgenic expression of Fhod3 in the heart sufficiently rescued the cardiac defects of Fhod3-null embryos but did not restore defects in neural tube closure, leading to exencephaly at the late embryonic stage (26). Fhod3 is therefore expected to play a crucial role also in neural tube closure, although the detailed mechanisms remain unclear.

This work was supported in part by Grants-in-aid for Scientific Research (C) JP18K06701 (to T. N.) and JP26460371 (to R. T.) from the Japan Society for the Promotion of Science (JSPS); a Grant-in-aid for Scientific Research on Innovative Areas, "Platform of Advanced Animal Model Support," (to R.T.) from the Ministry of Education, Culture, Sports, Science, and Technology (MEXT); the joint research program of the Biosignal Research Center, Kobe University (to R. T.); the President's Strategic Priority Budget of the University of Miyazaki (to R. T.); and a scholarship from the Otsuka Toshimi Scholarship Foundation (to H. W. S.). The authors declare that they have no conflicts of interest with the contents of this article.

[1] To whom correspondence should be addressed. E-mail: takeya@med.miyazaki-u.ac.jp.

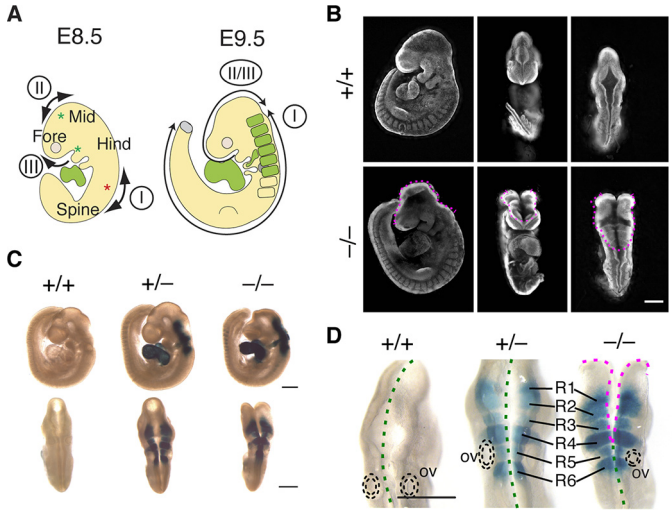

Figure 1. Fhod3 expression in rhombomeres 1–6 within the hindbrain. *A*, schematic representation of the cranial neural tube closure in mouse embryos. Closure I occurs from the hindbrain/spinal boundary (*red asterisk*) and proceeds bidirectionally. Closures II and III begin at the forebrain/midbrain boundary and the rostral end of the neural plate, respectively (*green asterisks*). By E9.5, the caudally directed closure II/III meets the rostrally directed closure I to seal the midbrain-hindbrain region. For details, see the Result section. Fhod3 is expressed in the heart and rhombomeres within the hindbrain region (*green*) during the neural tube closure. *Fore*, forebrain; *Mid*, midbrain; *Hind*, hindbrain. *B*, whole-mount nuclear fluorescent staining of *Fhod3*$^{+/+}$ (+/+) and *Fhod3*$^{-/-}$ (−/−) embryos at E9.5. The open regions of the cranial neural tube are indicated by *magenta dotted lines*. *Scale bar*, 500 μm. *C* and *D*, whole-mount *lacZ* staining of *Fhod3*$^{+/+}$, *Fhod3*$^{+/-}$, and *Fhod3*$^{-/-}$ embryos at E9.5. Open and closed regions are indicated by *magenta* and *green dotted lines*, respectively. *R1–6*, rhombomeres 1–6; *ov*, otic vesicle. *Scale bars*, 500 μm.

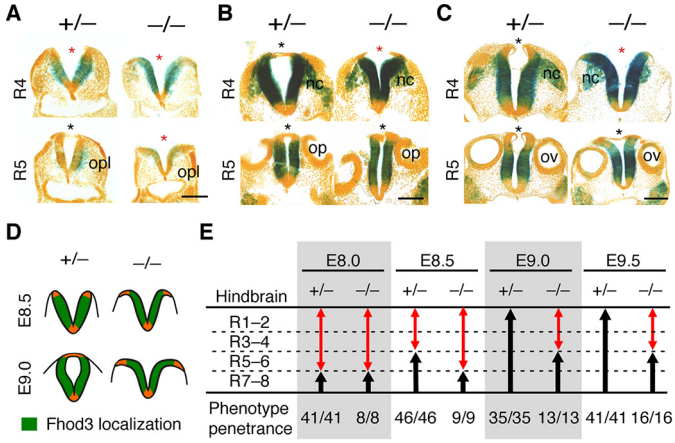

Figure 2. Fhod3 expression and morphological changes of the lateral neural plates in the hindbrain in *Fhod3*$^{-/-}$ embryos. *A–C*, *lacZ* staining of transverse sections of *Fhod3*$^{+/-}$ (+/−) and *Fhod3*$^{-/-}$ (−/−) embryos. Transverse sections at the level of rhombomeres 4 and 5 of *lacZ*-stained embryos at E8.5 (*A*), E9.0 (*B*), and E9.5 (*C*) are shown. Open and closed roof plates are indicated by *red* and *black asterisks*, respectively. *opl*, otic placode; *op*, otic pit; *ov*, otic vesicle; *nc*, migratory neural crest. *Scale bars*, 100 μm. *D*, schematic representation of Fhod3 expression and morphological changes of the lateral neural plates at the level of rhombomere 4. *E*, quantitative analysis of progression of rostral closure I. Open and closed regions are indicated by *red* and *black arrows*, respectively. The *number* of embryos in which the rostral zipping edge is present at each rhombomere level is shown. *R1–8*, rhombomeres 1–8.

In the present study, we examined the role of Fhod3 in neurulation during mouse embryonic development. The Fhod3 expression was restricted to the lateral plate of the neural tube at the level of rhombomeres 1 to 6 of the hindbrain. Fhod3-mediated apical constriction at the lateral plate contributed not only to mediolateral bending, to advance tube closure, but also to the anteroposterior bending associated with rhombomere bulging. The present findings provide direct evidence that a mammalian formin participates in epithelial morphogenesis during the embryonic developmental stage.

Results

Loss of Fhod3 prevents the rostrally directed closure of the neural tube at the hindbrain

To clarify the role of Fhod3 during neural development in mice, we examined the effect of Fhod3 deficiency on neurulation. In mice, neural tube closure is initiated at several different points (Fig. 1*A*). Around embryonic day E8.0, the initial closure (closure I) starts at the hindbrain/spinal boundary and proceeds both rostrally toward the head and caudally toward the tail. Subsequently, closures II and III begin at the forebrain/midbrain boundary and the rostral end of the neural plate, respectively. Closure II is sometimes absent, but closure III can proceed caudally instead of closure II (27). By E9.5, the caudally directed closure II/III meets the rostrally directed closure I at the midbrain/hindbrain boundary region, thus completing cranial neural tube closure. In Fhod3-null embryos at E9.5 (Fig. 1*B*), when cranial neural tube closure is normally complete, the caudally directed closure II/III and the rostrally directed closure I were aborted midway through the completion of the closure.

We then examined the Fhod3 expression by *lacZ* staining of heterozygous *Fhod3*$^{+/-}$ and homozygous *Fhod3*$^{-/-}$ embryos. As shown in Fig. 1*C*, the Fhod3 expression in the neural tube was restricted to the hindbrain, where closure I proceeds rostrally; no expression was observed in the midbrain or forebrain region, suggesting that Fhod3 depletion primarily affects rostrally directed closure I at the hindbrain. In the magnified dorsal view (Fig. 1*D*), the Fhod3 expression in the hindbrain exhibited a segmented pattern; *lacZ* staining was observed only in rhombomeres but not in the inter-rhombomere boundaries. Judging from the position of the otic vesicle, a morphological landmark for rhombomere 5, we concluded that Fhod3 was expressed specifically in rhombomeres 1 to 6. When compared with heterozygous *Fhod3*$^{+/-}$ embryos, in which closure was completed normally, the rostral closure in the Fhod3-null embryos ceased among these rhombomeres, suggesting the direct involvement of Fhod3 in rostrally directed closure I at the level of rhombomeres.

Loss of Fhod3 causes the morphological changes in the shape of the lateral neural plate

We next examined the Fhod3 expression in transverse sections of the hindbrain region and its relevance to the rostrally directed closure I (Fig. 2). In heterozygous control embryos (Fig. 2, *A–C*, *left panels*), Fhod3 was expressed robustly in the closing neural plate. Notably, Fhod3 expression was restricted to the lateral plate and completely absent from the floor and roof plates of the neural tube. In Fhod3-null embryos (Fig. 2, *A–C*, *right panels*), the distribution pattern was essentially the same, but the shape of the neural plate was strikingly different

from that of the controls (Fig. 2, *A*–*C*; represented schematically in Fig. 2*D*). In control embryos at E8.5, the neural plate at the level of rhombomere 4 was folded at the midline, forming a V-shaped neural groove. By E9.0, the bilateral neural plates bent dorsomedially toward the midline; the ridges of the neural plates were then flipped and fused. In null embryos at E8.5, the bilateral neural plates were not straight but convex, with their dorsal ridges orientated away from the midline. At E9.0, the bilateral plates never bent toward the midline, leaving the dorsal ridges still separated from each other at E9.5. Although Fhod3 was also expressed in migrating neural crest cells, migration from rhombomere 4 appeared to occur normally. We summarized the failure of rostral progression of closure I in the hindbrain of Fhod3-null embryos in Fig. 2*E*. The rostrally directed closure occurred normally in rhombomeres 7–8 where *lacZ* staining is negative. The closure was delayed in rhombomeres 5–6 and never proceeded further. Notably, as shown in Fig. 2*C*, the fusion of the roof plate of Fhod3-null embryos occurred at rhombomere 5 but not at rhombomere 4, despite the fact that the lateral plate bending was impaired at both rhombomeres. This is probably because the fusion of the roof plate is an event that is independent from the bending of the lateral plates (27). These phenotypes showed full penetration in all Fhod3-null embryos examined. It therefore seems that Fhod3 depletion causes morphological changes in lateral neural plates, thereby resulting in abortion of rostrally directed closure I, which is most evident at the level of rhombomere 4.

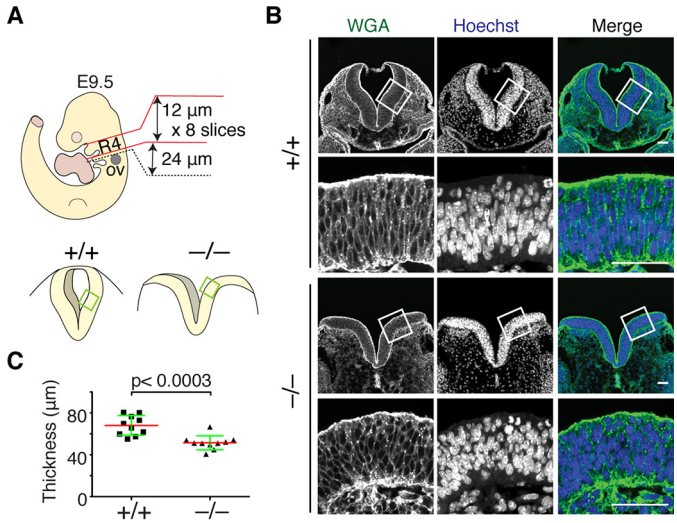

Figure 3. Abnormal organization of neuroepithelial cells in the lateral neural plates of *Fhod3*$^{-/-}$ embryos. *A*, schematic representation of the orientation of transverse sections used in *B* and in Figs. 4 and 5. Transverse sections at the level of rhombomere 4 were defined by their position relative to the otic vesicle (*ov*). *B*, confocal fluorescence micrographs of the hindbrain of *Fhod3*$^{+/-}$ (+/−) and *Fhod3*$^{-/-}$ (−/−) embryos at E9.5. Transverse sections at the level of rhombomere 4 were subjected to fluorescence staining for the plasma membrane with WGA (*green*) and for the nucleus with Hoechst (*blue*). *Scale bars*, 50 μm. *C*, quantification of neural plate height. The height (distance from apical to basement membrane) of lateral neural plates was measured at the cropped region of *Fhod3*$^{+/+}$ and *Fhod3*$^{-/-}$ embryos at E9.5 (n = 10 mice/genotype). Data are shown as mean (*red line*) ± S.D. (*green lines*).

Fhod3 is required for proper columnar organization of neuroepithelial cells

To analyze morphological changes in the neural plates in Fhod3-null embryos, we examined the cellular organization of the neuroepithelium at the level of rhombomere 4 of E9.5 embryos, where the morphological changes are most evident. Transverse sections were stained with wheat germ agglutinin (WGA),[2] which intensely labels the cellular surface of neuroepithelial cells (28). As shown in Fig. 3*A*, the neural plate of WT embryos formed a tightly packed pseudostratified columnar epithelium with a flat apical surface. In contrast, the neural plate of Fhod3-null embryos failed to form a columnar epithelium, and the cells did not become compacted into a regular packed pattern. The flatness of the apical surface was considerably disturbed, and the height of the neural plate was significantly shorter than in WT embryos (Fig. 3*B*). As such a shortage in height has been observed in rat embryos exposed to cytochalasin D (29) as well as mouse mutant embryos that show neural tube defects due to affecting F-actin organization, such as *Shroom3*, *NUAK1/2*, and *Cofilin* mutants (30–32), Fhod3 is expected to contribute to the organization of pseudostratified neuroepithelial cells via the regulation of F-actin–mediated constriction (33, 34). In addition, the nuclear shape of neuroepithelial cells was largely influenced by Fhod3 depletion (Fig. 3*A*), although there were no significant differences in cell number per length of basement membrane (WT, 90.25 ± 8.56 cells; Fhod3-null, 109.3 ± 8.17 cells; p = 0.14). Nuclear positioning and shaping in pseudostratified epithelia are also dynamically controlled by actomyosin contractility in a cell cycle–dependent manner (35). It thus seems likely that Fhod3-mediated actin organization is involved in the columnar organization of neuroepithelial cells.

Fhod3 is required for F-actin assembly at the apical surface of neuroepithelial cells

To identify the effect of Fhod3 depletion on F-actin organization in neuroepithelial cells, we analyzed F-actin distribution in neuroepithelial cells at the level of rhombomere 4 of E9.5 embryos. In WT embryos, F-actin was accumulated at the apical surface of the lateral neural plates (Fig. 4*A*), which is evident in pixel intensity quantification along an apicobasal trace of 30 μm in width (Fig. 4*B*). By contrast, the apical accumulation of F-actin at the convex surface of bilateral neural plates of Fhod3-null embryos was significantly decreased, although the intensity at the lateral membranes was not substantially altered (Fig. 4*C*). The tight junction protein ZO-1 at the convex surface was also decreased, although accumulation was detectable (Fig. 4, *A* and *B*).

On the other hand, the adherens junction protein cadherin at the apical surface and lateral contacts was not substantially altered, suggesting that adherens junctions are better retained (Fig. 5*A*). We then estimated the force in cadherin-mediated junctions using the mAb α18, which recognizes the force-induced active conformation of α-catenin, a linker molecule between cadherin and F-actin (36). In WT embryos, activated α-catenin was accumulated at the apical surface of the lateral plate, where myosin heavy chain was also accumulated (Fig. 5*B*, *MHC IIB*). In contrast, the accumulation of the α18 signal at the

[2] The abbreviations used are: WGA, wheat germ agglutinin; PCP, planar cell polarity; PFA, paraformaldehyde.

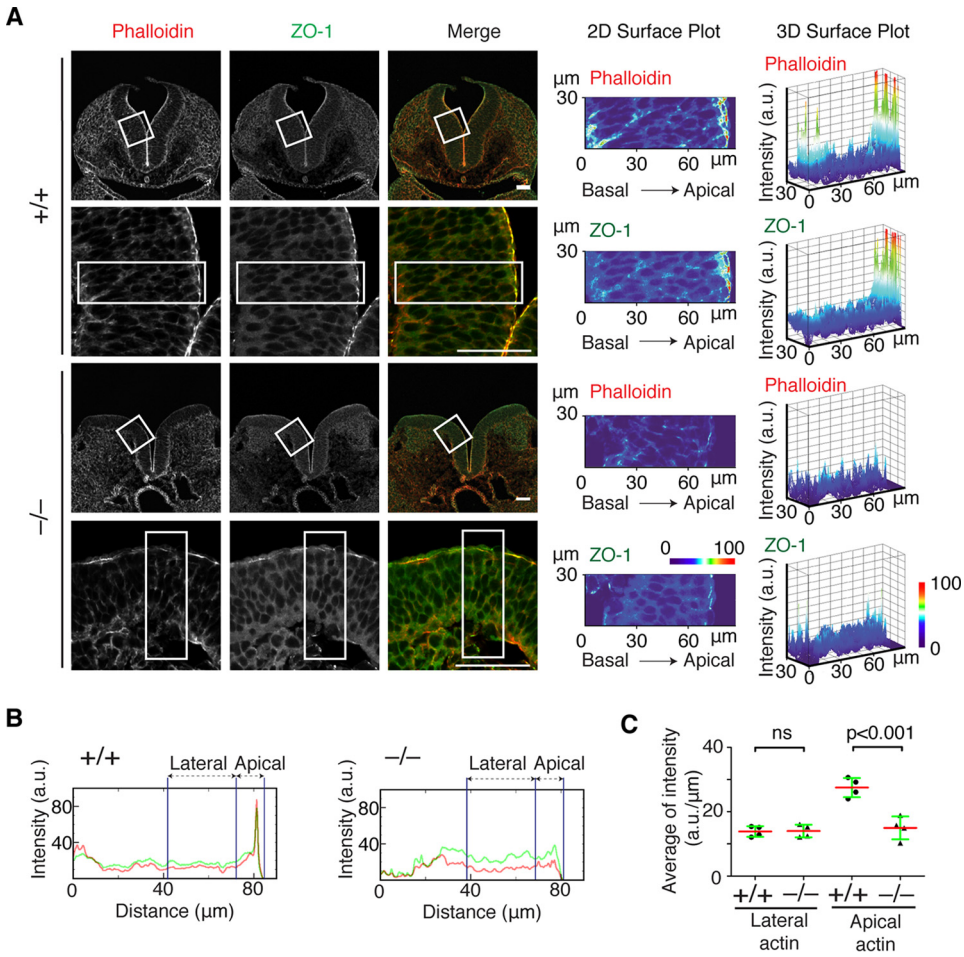

Figure 4. F-actin assembly at the apical surface of the lateral neural plates of *Fhod3*$^{-/-}$ embryos. *A*, confocal fluorescence micrographs of the hindbrain of *Fhod3*$^{+/+}$ (+/+) and *Fhod3*$^{-/-}$ (−/−) embryos at E9.5. Transverse sections at the level of rhombomere 4 were subjected to immunofluorescence staining for ZO-1 (*green*) and phalloidin staining for F-actin (*red*). *Scale bars*, 50 μm. Two- and three-dimensional surface plots of the intensity of pixels of boxed regions were shown on a pseudocolor scale. *B*, pixel intensity profiles of phalloidin (*red*) and ZO-1 (*green*) along apicobasal traces (*boxed* in *A*) of lateral neural plates of *Fhod3*$^{+/+}$ and *Fhod3*$^{-/-}$ embryos at E9.5. *C*, quantification of the pixel intensities of the apical and lateral F-actin. The average fluorescence intensity at the apical domain (within 12 μm of the apical surface) and lateral domain (12–42 μm from the apical surface) was calculated from pixel intensity profiles of *Fhod3*$^{+/+}$ ($n = 4$ images from 3 embryos) and *Fhod3*$^{-/-}$ embryos ($n = 4$ images from 3 embryos) as shown in *A*. Data are shown as mean (*red line*) ± S.D. (*green lines*). *ns*, not significant.

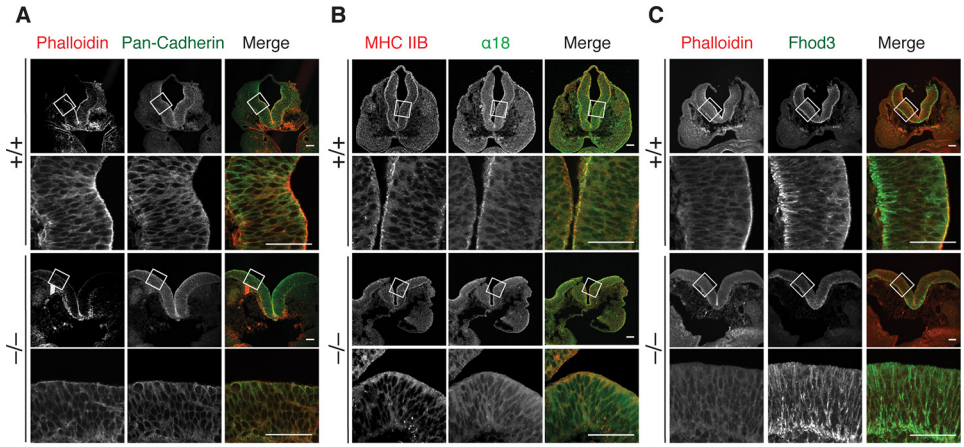

Figure 5. Formation of the apical junctional complex in the lateral neural plates of *Fhod3*$^{-/-}$ embryos. Confocal fluorescence micrographs of the hindbrain of *Fhod3*$^{+/+}$ (+/+) and *Fhod3*$^{-/-}$ (−/−) embryos at E9.5. Transverse sections at the level of rhombomere 4 were subjected to immunofluorescence staining for pan-cadherin (*green*) and phalloidin staining for F-actin (*red*) (*A*), for myosin heavy chain IIB (*MHC IIB*, *red*) and activated α-catenin (*green*) (*B*), and for Fhod3 (*green*) and phalloidin staining for F-actin (*red*) (*C*). *Scale bars*, 50 μm.

apical surface was attenuated in null embryos. We further investigated the subcellular localization of Fhod3 (Fig. 5*C*). Although the Fhod3 antibody used cross-reacted significantly with filamentous structures abundant in the basal region of neuroepithelial cells, the apical accumulation of endogenous Fhod3 was detected specifically in WT embryos. Thus, we con-

cluded that Fhod3 localizes to the apical surface of neuroepithelial cell and its depletion causes the loss of F-actin preferentially at the apical surface, thereby seemingly affecting the apical surface tension.

Fhod3 is required for the organization of the apical junctional complex of neuroepithelial cells

To further examine the apical junctional complex, transmission electron microscopic analysis was performed. In WT embryos, electron-dense junctional complexes could be seen (Fig. 6, *A* and *B*, *upper panels*) as reported in previous studies (29, 37). In Fhod3-null embryos, cell–cell contacts (*i.e.* electron-dense membrane specializations) were retained (Fig. 6, *A* and *B*, *lower panels*) but were sparsely distributed when compared with those in WT embryos, suggesting the loss of contraction of the apical plane. This loosely organized pattern is also observed in scanning electron microscopic images (Fig. 6*C*). In some areas, apical cell–cell contacts appeared to be loosened in Fhod3-null embryos (the *green arrow* in Fig. 6*A*). Because the linkage with F-actin is required for strong homophilic interactions of cadherins (38), the loss of F-actin might affect the integrity of apical junctions, although lateral membrane contacts are still retained. Fhod3 depletion thus causes the loss of apical F-actin, thereby affecting the organization of the apical junctional complex of neuroepithelial cells.

Loss of Fhod3 induces enlargement of the apical surface area of the lateral neural plate

To clarify whether the loss of apical F-actin actually causes the failure of apical constriction, we observed the apical surface of the lateral neural plate using sections tangential to the apical plane (Fig. 7*A*). Although phalloidin and ZO-1 signals were considerably reduced in Fhod3-null embryos, ZO-1 was distributed circumferentially around the cell, allowing us to measure the area of the apical surface of the cell (Fig. 7*B*). The surface area at the apical plane of the lateral neural plate, outlined by ZO-1 staining, in Fhod3-null embryos was more than twice as large as that of WT embryos, indicating reduced apical constriction (Fig. 7*C*). The reduction of apical constriction, *i.e.* enlargement of the surface area, was also observed in the whole-mount analysis of the lateral neural plate, in which we were able to determine the axial orientation of the anteroposterior and mediolateral axes (Fig. 7, *D–F*). It has been reported that, at the floor plate of the bending neural tube in chicken embryos, neuroepithelial cells adopt rectangular shapes, with their long axes lying along the anteroposterior axis of the embryo (39); this shape seems to be the result of planar-polarized contraction of junctional actomyosin toward the mediolateral axis, thereby enabling the plate to bend along the anteroposterior axis of the embryo. Remarkably, the apical junction pattern in rhombomere regions of the lateral plate of the mouse neural tube showed an almost isotropic honeycomb-like arrangement and not a rectangular shape, although in boundary regions it appeared as elongated shapes, with their long axes along the mediolateral axis (Fig. 7, *G* and *H*) This isotropic pattern raises the possibility that nonpolarized isotropic contraction occurs in rhombomere regions at the lateral plate of the mouse neural tube.

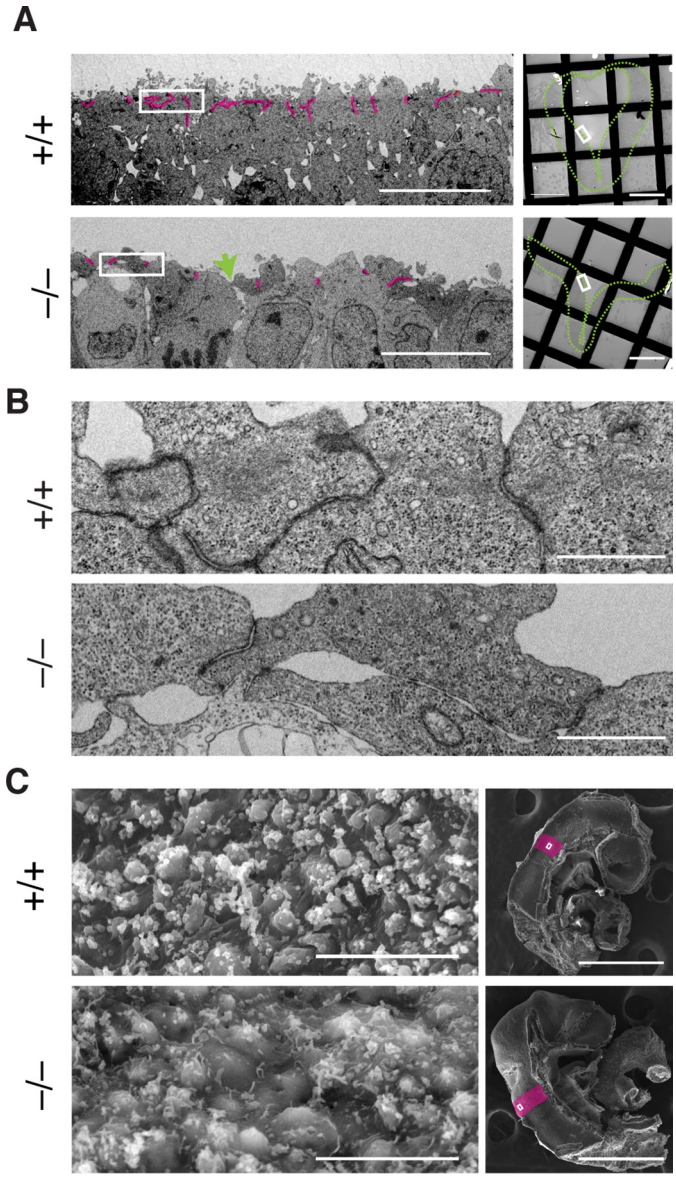

Figure 6. The ultrastructure of the lateral neural plate of *Fhod3*$^{-/-}$ embryos. *A*, transmission electron micrographs of thin sections of the apical surface of the lateral neural plates in *Fhod3*$^{+/+}$ (+/+) and *Fhod3*$^{-/-}$ (−/−) embryos at E9.5. Cell–cell contacts (*i.e.* electron-dense membrane specializations) are highlighted in *magenta*. The *green arrow* indicates a loosened apical cell–cell contact. The orientation of the images in the *left panels* is shown as *white boxes* in *right panels*. The *outlines* of neural plates are indicated by *green dotted lines*. *Scale bars*, 10 μm (*left panels*) and 100 μm (*right panels*). *B*, examples of electron-dense membrane specializations are enlarged from images shown in *A*. *Scale bars*, 1 μm. *C*, scanning electron micrographs of the apical surface of the lateral neural plates in *Fhod3*$^{+/+}$ and *Fhod3*$^{-/-}$ embryos at E9.5. The orientation of images in the *left panels* is shown as *white boxes* in the *right panels*. Rhombomere 4 is indicated in *magenta*. *Scale bars*, 10 μm (*left panels*) and 500 μm (*right panels*).

Fhod3 is required for morphological segmentation of rhombomeres

We therefore examined whether or not the apical constriction occurs not only toward the mediolateral axis but also the anteroposterior axis at the lateral plate of the mouse neural tube. To this end, we optically sectioned the apical surface of the lateral neural tube of the whole-mount embryos in the anteroposterior plane by confocal microscopy (Fig. 8*A*). Apical F-actin was accumulated in the center of rhombomeres (shown

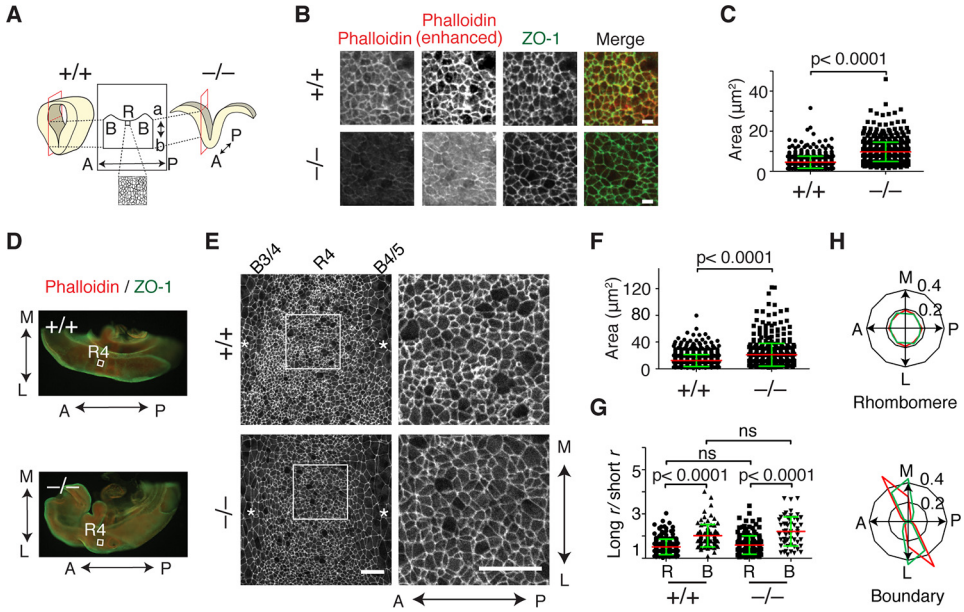

Figure 7. Apical constriction in the lateral neural plate of *Fhod3*$^{-/-}$ embryos. *A*, schematic representation of the orientation of sagittal sections tangential to the apical plane used in *B* (*B*, boundary; *R*, rhombomere; *a*, apical; *b*, basal; *A*, anterior; *P*, posterior). *B*, apical view of the lateral neural plate at the level of rhombomere 4 in the hindbrain of *Fhod3*$^{+/+}$ (+/+) and *Fhod3*$^{-/-}$ (−/−) embryos at E9.5. Sections were subjected to immunofluorescence staining for ZO-1 (*green*) and phalloidin staining for F-actin (*red*). *Scale bars*, 5 μm. *C*, quantification of apical cell surface area of sagittal sections. The apical surface area was estimated by ZO-1 staining of sections prepared from *Fhod3*$^{+/+}$ ($n = 630$ cells from 4 embryos) and *Fhod3*$^{-/-}$ embryos ($n = 758$ cells from 4 embryos) shown in *A*. *D*, whole-mount staining of embryo halves. E9.5 embryos bisected at the midline were subjected to immunofluorescence staining for phalloidin (*red*) and ZO-1 (*green*). *R4*, rhombomere 4. *E*, apical view of whole-mount staining of ZO-1 at rhombomere 4 in the hindbrain from *Fhod3*$^{+/+}$ and *Fhod3*$^{-/-}$ embryos at E9.5. *Asterisks* indicate inter-rhombomere boundaries. *A*↔*P*, anterior to posterior; *M*↔*L* medial to lateral. *Scale bars*, 25 μm. *F*, quantification of apical cell surface area of whole-mount embryos. The apical surface area was estimated by ZO-1 staining of whole-mount *Fhod3*$^{+/+}$ ($n = 844$ cells from 3 embryos) and *Fhod3*$^{-/-}$ embryos ($n = 532$ cells from 3 embryos) shown in *E*. *G*, the anisotropy of the apical junction pattern. Cell outlines defined by ZO-1 staining shown in *E* were fitted to an elliptical shape, estimated by the ratio of the long to short radius (*r*) (rhombomere of *Fhod3*$^{+/+}$, $n = 224$ cells from 3 embryos; boundary of *Fhod3*$^{+/+}$, $n = 88$ cells from 3 embryos; rhombomere of *Fhod3*$^{-/-}$, $n = 178$ cells from 3 embryos; boundary of *Fhod3*$^{+/+}$, $n = 55$ cells from 3 embryos). For details, see "Experimental procedures." *R*, rhombomere; *B*, boundary; *ns*, not significant. Data are shown as mean (*red line*) ± S.D. (*green lines*). *H*, polar plots representing orientation of long-axis angles of cell outlines defined by ZO-1 staining shown in *E*. (*red*, *Fhod3*$^{+/+}$; *green*, *Fhod3*$^{-/-}$). *A*↔*P*, anterior to posterior; *M*↔*L* medial to lateral.

in Fig. 8*B*), as observed in chick embryos in previous studies (40, 41). Notably, neuroepithelial cells in the central region of the rhombomere constricted apically toward the center of the rhombomere. In contrast, F-actin was distributed evenly in Fhod3-null embryos, and no constriction pattern was observed. It therefore seems that Fhod3 promotes anteroposterior-oriented apical constriction by inducing the rhombomere-specific accumulation of F-actin. Consistent with this idea, longitudinal sections of the neural tube in WT embryos showed uneven F-actin distribution along the anteroposterior axis; the intensity of apical F-actin in the rhombomere regions was relatively high compared with that in boundary regions (Fig. 8*C*). Nuclear staining in WT embryos also exhibited a segmented pattern, whereas such a pattern was not evident in null embryos. In addition, whole-mount dorsolateral views of the hindbrain showed that outward bulging of rhombomeres was less prominent in Fhod3-null embryos than in the WT (Fig. 8, *D* and *E*). Thus, contraction along the anteroposterior axis at the lateral plate, caused by the Fhod3-dependent accumulation of apical F-actin at the rhombomere centers, seems to be responsible for the morphological segmentation of rhombomeres.

Discussion

In the present study, we identified the critical role of Fhod3 in neurulation during mouse embryonic development. In neuroepithelial cells of the hindbrain, Fhod3 regulates F-actin assembly at the apical junctional complex to promote apical constriction, thereby bending the neural plate, as we expected from previous *in vivo* studies of invertebrate and avian formins as well as from findings in *in vitro* models of mammalian formins. However, somewhat unexpectedly, Fhod3-mediated apical constriction occurred only at the lateral plate, seeming to contribute to both the mediolateral and anteroposterior bending associated with tube closure and rhombomere bulging, respectively. To our knowledge, this is the first study showing that a mammalian formin contributes to epithelial morphogenesis, especially rhombomeric organization, during embryonic development.

Although neural tube closure is a paradigm for explaining epithelial morphogenesis in vertebrates, the cellular mechanisms involved seems to vary across species as well as across axial levels (*i.e.* cranial *versus* spinal) (2). In rodents, it is known that cranial neural tube closure is sensitive to the inhibition of F-actin assembly, whereas spinal neurulation is relatively resistant (29, 37). Accordingly, the shape of the closing neural tube in the transverse plane differs among axial levels (2, 42). In the upper hindbrain of rodent embryos, the lateral neural plates undergo sequential changes in shape as follows: convex neural folds are formed first, subsequently flattening into a V-shape with an increase in cell height and then becoming concave prior to neural tube closure (43). This sequence of changes in lateral

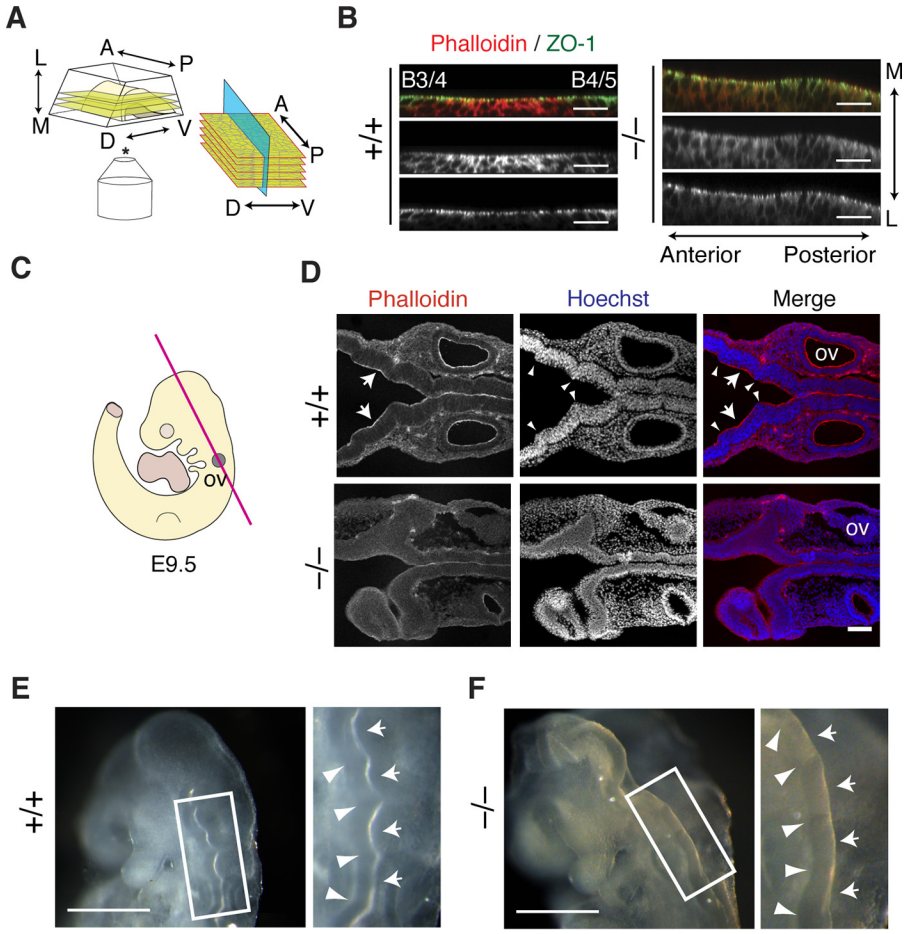

Figure 8. Effects of Fhod3 depletion in morphological segmentation of rhombomeres. *A*, schematic representation of the orientation of optical sectioning of whole-mounted neural tubes embedded in an agarose gel used in *B*. *B*, orthogonal projection of Z-stack slices of whole-mounted neural tubes at rhombomere 4 in the hindbrain of *Fhod3*$^{+/+}$ (+/+) and *Fhod3*$^{-/-}$ (−/−) embryos at E9.5. Whole-mount embryos were subjected to immunofluorescence staining for ZO-1 (*green*) and F-actin (*red*) (*B*, boundary). *Scale bars*, 100 μm. *C*, schematic representation of the orientation of longitudinal coronal sections used in *D*. *D*, longitudinal coronal sections of the hindbrain of *Fhod3*$^{+/+}$ and *Fhod3*$^{-/-}$ embryos at E9.5. Sections were subjected to fluorescence staining for F-actin (*red*) and nucleus (*blue*). Inter-rhombomere boundaries are indicated by *arrowheads*. *Scale bars*, 100 μm. *E* and *F*, whole-mount images of *Fhod3*$^{+/+}$ (*E*) and *Fhod3*$^{-/-}$ (*F*) embryos at E9.5 in lateral and dorsal views (*left* and *right*, respectively). Inter-rhombomere boundaries and rhombomere bulges are indicated by *arrowheads* and *arrows*, respectively. *Scale bars*, 500 μm.

plate shape is accompanied by a contraction of the apical F-actin network (29, 33, 34). In Fhod3-null embryos, the series of shape changes is completely aborted, and both lateral plates retain their convex curvature (Fig. 2). The Fhod3-mediated F-actin assembly at the apical surface seems to be responsible for this morphological process of the lateral plate by generating tension at the apical junctions.

In chicks, Daam1, a member of the formin family, is expressed in the ventral half of the closing neural tube (44) and seems to be essential for its bending at the midline by promoting apical constriction (39). In contrast, at least in mice, the expression of Daam1 and Daam2 was not detected in the neural tube until E10.5, when the neural tube closure was completed (44). This suggests a dispensable role of Daam1 and 2 on neural tube closure in mice, which is also supported by the lack of any significant defects in neural tube closure in Daam1-deficient mice (45). It therefore seems that different formins participate in different shape changes in neural plates in different vertebrates, although a formin-dependent mechanism is obviously pivotal to neural tube closure in vertebrates.

It has recently been reported that in mouse mammary-gland epithelial cells, Daam1 specifically localizes to lateral membranes rather than the apical junctional complex and its depletion causes loss of lateral F-actin but does not affect the apical F-actin (24). Daam1 thus functions in regulating the lateral F-actin, at least in mammary epithelium. By contrast, we showed in the present study that Fhod3 localizes to the apical region (Fig. 5) and its depletion induces the significant loss of apical F-actin (Figs. 4 and 6); the specific localization of Fhod3 to the apical junctional complex has very recently been reported also in *Xenopus* gastrula epithelium (46). Fhod3 thus appears to control primarily the formation of the apical F-actin, although it also may affect the lateral F-actin, as both networks are expected to be mutually interdependent (47).

During embryonic development, the vertebrate hindbrain is transiently divided into rhombomeres, a series of bulging segments of the neural tube along the anteroposterior axis (48, 49). The segmental identity of rhombomeres is specified by the combinatorial expression of selector genes, such as the *Hox* genes (49–51). By contrast, the morphological segmentation of

rhombomeres seems to be regulated by the actin cytoskeleton (51, 52). In the parasagittal plane of the chick hindbrain, neuroepithelial cells within the inter-rhombomere boundaries are wedge-shaped, with their apical surface expanding outward, whereas their basal ends, enriched with F-actin, are constricted (40). Rhombomere regions, in contrast, display complementary morphology; their apical surfaces are constricted with the strong accumulation of F-actin, prompting invagination of the apical region (40). Little is known, however, about the actin regulator responsible for this rhombomere-specific accumulation of F-actin. The present findings that rhombomeric distribution of apical F-actin and segmental bulging of the neural tube were attenuated in Fhod3-null embryos strongly support the idea that physical force generated by apical constriction along the anteroposterior axis is responsible for the morphological segmentation of rhombomeres and that Fhod3 is a key regulator of the rhombomere-specific F-actin assembly. Consistent with our observation, Filas *et al.* (41) suggest, using computational modeling, that rhombomere bulging requires contractile force along the anteroposterior axis at the apical surface of rhombomeres. Fhod3-mediated apical constriction in the anteroposterior axis therefore seems to contribute to the morphological segmentation of rhombomeres.

Rhombomere segmentation in the hindbrain is precisely controlled spatially and temporally. Although the entire hindbrain can be divided into 11 rhombomeres, the caudal region of the hindbrain (*i.e.* rhombomeres 7–11) is not overtly segmented (53). The well-segmented rhombomeres 1–6 in the upper hindbrain become obvious only from approximately E8.5 and eventually disappear by E11.5. In accordance with this location and time course, Fhod3 expression in rhombomeres 1–6 becomes visible from E8.5 but subsequently disappears by E11.5 (26), suggesting that Fhod3 is committed to the transient appearance of rhombomeres. Tropomyosin, a coiled-coil actin-binding protein (54), is expressed at inter-rhombomere boundaries in the developing hindbrain (55) in a manner complementary to Fhod3. Tropomyosin expression at boundaries also disappears almost synchronously with the disappearance of rhombomeres (55). These different types of actin regulators, one specific to the rhombomere and one specific to the boundary, might cooperate spatially and temporally to execute morphological segmentation of rhombomeres.

It has been reported that, in chicks, the planar cell polarity (PCP)–controlled anisotropic apical constriction, which involves the polarized activation of ROCK and Daam1 of the formin family, causes polarized bending of the cranial neural tube toward the mediolateral direction at the midline (39). By contrast, in the present study, we show that Fhod3-mediated apical constriction of neural plate cells was polarized not only toward the mediolateral axis but also the anteroposterior axis, causing bidirectional bending along both axes. Thus, at least in the lateral plates of the neural tube, apical constriction seems to occur multidirectionally. However, it is still possible that Fhod3-mediated apical constriction is also controlled by PCP signaling, because rhombomere morphogenesis requires precise coordination between the neural plate bending and convergent extension movement, which depends on the PCP signaling (39, 56). Future studies are awaited to elucidate the detailed mechanism, including investigations into a molecular link between Fhod3-mediated F-actin assembly and the PCP pathway.

Experimental procedures

Mice

The *Fhod3* knockout mice were generated by replacing exon 1 with *lacZ* as described previously (26). To obtain timed pregnancies, paired female mice were checked daily in the morning, and the day of vaginal plug formation was termed E0.5. Pregnant mice were sacrificed on a designated day, and embryos were dissected from the uterus followed by PCR genotyping using yolk sac DNA as described previously (26).

All experimental protocols were approved by the Animal Care and Use Committee of Miyazaki University (permit No. 2014-526-3). All mice were housed and maintained in a specific pathogen-free animal facility at the University of Miyazaki, and all efforts were made to minimize the number of animals used and their suffering. All experiments were performed in strict accordance with the guidelines for Proper Conduct of Animal Experiments (Science Council of Japan) and the *Guide for the Care and Use of Laboratory Animals* published by the U. S. National Institutes of Health.

LacZ staining

LacZ staining was performed as described previously with minor modification (26, 57). Briefly, whole mice embryos were fixed at 4 °C by immersion in PBS (137 mM NaCl, 2.68 mM KCl, 8.1 mM Na_2HPO_4, and 1.47 mM KH_2PO_4, pH 7.4) containing 1% formaldehyde, 0.2% glutaraldehyde, 0.02% Nonidet P-40, and 1 mM $MgCl_2$ for 3 h. The fixed embryos were incubated at 37 °C in PBS containing 1 mg/ml X-Gal, 5 mM $K_3Fe(CN)_6$, 5 mM $K_4Fe(CN)_6$, and 2 mM $MgCl_2$. All embryos were post-fixed overnight at 4 °C in 3.7% paraformaldehyde (PFA) in PBS and then immersed at 4 °C in 30% sucrose. Cryosections were performed at 30 μm thickness followed by counter staining with 1% Orange G (WAKO) in 2% phosphotungstic acid.

Whole-mount nuclear fluorescent staining

Whole-mount nuclear fluorescent staining was performed as described (58). Briefly, mice embryos were fixed at 4 °C overnight in 3.7% PFA in PBS and then incubated in Hoechst 33342 for 20 min at room temperature. Samples were washed with PBS and observed under a BZ-9000 microscope. Images were constructed by merging Z-stack frames into a single projection.

Antibodies

Rabbit polyclonal antibodies for Fhod3 (anti-Fhod3-(650–802)) were prepared as described previously (59). The rat anti-α-catenin mAb α18 (36) was a kind gift from Dr. Akira Nagafuchi (Nara Medical University). The following antibodies were purchased: mouse anti-ZO-1 clone ZO1-1A12 (Thermo Fischer Scientific); mouse anti-pan-cadherin clone CH-19 (Santa Cruz Biotechnology); rabbit anti-nonmuscle myosin heavy chain IIB (Covance); Alexa Fluor 555–conjugated $F(ab')_2$ fragment of anti-rabbit IgG (Cell Signaling Technology); Alexa Fluor 488–conjugated $F(ab')_2$ fragment of anti-mouse IgG (Cell Signaling Technology); and Alexa Fluor 488–conjugated anti-rat IgG (Thermo Fisher Scientific). Actin filaments were

stained with Alexa Fluor 555–phalloidin (Invitrogen). Nuclei were stained with Hoechst 33342 (Dojindo). Cell membranes were stained with FITC-labeled WGA (J-Oil Mills, Inc.). Images were taken with a LSM700 (Carl Zeiss Micro Imaging) or TCS SP8 (Leica) confocal scanning laser microscope.

Immunofluorescence staining

Immunofluorescence staining was performed as described previously with minor modification (26). Timed pregnant mice were euthanized by cervical dislocation, and embryos were collected. Mice embryos fixed overnight at 4 °C in 3.7% PFA in PBS followed by cryoprotection at 4 °C in 30% sucrose were embedded in colored tissue freezing medium (Triangle Biomedical Sciences). The blocks were frozen, and serial sections were obtained from the level of rhombomere 4 (thickness, 12 μm) using a cryostat CM3050S (Leica Biosystems). Sections were washed with PBS containing 0.1% Triton X-100, and blocked with PBS containing 3% BSA for 60 min at room temperature. Sections were labeled overnight at 4 °C with primary antibodies diluted in PBS containing 1% BSA, washed with PBS, and then labeled for 3 h at 4 °C with fluorescently labeled secondary antibody mixture in the same buffer. For staining with the α18 antibody, samples were fixed in 10% TCA in Tris-buffered saline (TBS: 150 mM NaCl and 20 mM Tris-HCl, pH 7.4) and treated in TBS-based buffer solution. Images were taken with a Zeiss LSM700 confocal microscope or Leica TCS SP8 confocal microscope under the same conditions between Fhod3-null and WT embryos.

Whole-mount staining was performed as described previously with minor modification (31). Briefly, the fixed embryos were cut into two halves at the midline, permeabilized for 10 min with PBS containing 0.1% Triton X-100, and blocked for 2 h with 3% BSA in PBS. The embryos were incubated with primary antibody overnight at 4 °C, washed three times for 30 min with PBS, incubated overnight at 4 °C with secondary antibody, and then washed five times with PBS for 30 min. Stained embryos were embedded with 1% low-melting-point agarose in PBS and put on a 35-mm glass-bottom culture dish. Images were taken with an LSM 700 confocal microscope under the same conditions between Fhod3-null and WT embryos unless noted otherwise.

Image analysis and quantification

Quantification of neural plate height and apical surface area was performed as described (32). Briefly, measurements of neural plate height were made by measuring distance from the apical to the basement membrane of the lateral neural plate. To estimate apical surface areas, sagittal sections tangential to the apical plane were stained with ZO-1, traced manually, and measured using ImageJ (National Institutes of Health) with Fiji plugins (60). The average number of cells/100 μm of neural plate basement membrane was obtained from the number of nuclei stained with Hoechst in transverse sections (five images from five embryos of each genotype).

Pixel intensity along the apicobasal axis was determined on confocal images acquired and processed under the same conditions between Fhod3-null and WT embryos. Three-dimensional surface plots and intensity profiles of pixel intensity were made from apicobasal traces (30 μm wide) of lateral neural plates using ImageJ. To quantify the apical and lateral F-actin, the average fluorescence intensity in the apical domain (within 12 μm of the apical surface) and lateral domain (12–42 μm from the apical surface) was quantified from the pixel intensity profiles.

Cell outlines in confocal images were automatically identified using a plugin in Image J (Automated Multicellular Tissue Analysis) developed by the Advanced Digital Microscopy Core Facility at the Institute for Research in Biomedicine (Barcelona, Spain). The outline of each cell was fitted into an ellipse, and the longitudinal and transverse axes were calculated automatically in ImageJ. The angles of each longitudinal axis with respect to the AP axis were grouped into bins of 30° and represented in polar plots symmetrically about the AP axis.

EM analysis

Transmission EM of thin sections was performed as described previously with minor modification (61). Briefly, timed pregnant mice were euthanized by cervical dislocation, and embryos were dissected in HBSS buffer (138 mM NaCl, 5.33 mM KCl, 4.17 mM $NaHCO_3$, 0.34 mM Na_2HPO_4, 0.44 mM KH_2PO_4, 1.26 mM $CaCl_2$, 0.49 mM $MgCl_2$, and 0.41 mM $MgSO_4$). Mouse embryos were immersed in the fixative solution (2.0% PFA, 2.5% glutaraldehyde, and 0.1 M sodium cacodylate, pH 7.4), and then the fixed tissue was rinsed in PBS, post-fixed in 1% osmium tetroxide, dehydrated in ethanol and propylene oxide, and embedded in epoxy resin. Thin sections stained with uranyl acetate and lead citrate were then examined with a HT7700 (Hitachi) transmission electron microscope. For EM scanning, the post-fixed samples were treated with 1% tannic acid and 1% osmium tetroxide for conductive staining and then dehydrated in ethanol. The samples were dried, mounted on aluminum stubs coated with gold/palladium using sputter coating, and then examined with an S-4800 (Hitachi) field emission scanning electron microscope.

Statistical analysis

Data were shown as mean ± S.D. A *t* test was conducted to determine the level of significance (*p* value of <0.05). Statistical analysis was performed using GraphPad Prism 5.0 (GraphPad Software Inc., San Diego, CA).

Author contributions—H. W. S., T. N., and R. T. conceptualization; H. W. S. data curation; H. W. S. formal analysis; H. W. S., T. N., and R. T. funding acquisition; H. W. S. investigation; H. W. S. and T. N. methodology; H. W. S. and R. T. writing-original draft; H. W. S., T. N., T. Y., and R. T. writing-review and editing; T. Y. and R. T. resources; T. Y. project administration; R. T. supervision.

Acknowledgments—We thank Dr. Akira Nagafuchi (Nara Medical University) for providing the α18 antibody, Dr. Takehiko Ueyama (Kobe University) for technical advice and helpful discussion, Dr. Honami Ogoh (University of Miyazaki) for advice on analysis of embryonic mice, Dr. Fumiyuki Sanematsu (University of Miyazaki) for advice on microscopic analysis, Yoshiteru Goto (University of Miyazaki) and Yohko Kage (University of Miyazaki) for electron microscopic analysis, and Asami Akiyama (University of Miyazaki) and Katsue Yokoyama (University of Miyazaki) for secretarial assistance. We also appreciate the technical support received from the Frontier Science Research Center, University of Miyazaki.

References

1. Wallingford, J. B., Niswander, L. A., Shaw, G. M., and Finnell, R. H. (2013) The continuing challenge of understanding, preventing, and treating neural tube defects. *Science* **339,** 1222002 CrossRef Medline
2. Nikolopoulou, E., Galea, G. L., Rolo, A., Greene, N. D., and Copp, A. J. (2017) Neural tube closure: Cellular, molecular and biomechanical mechanisms. *Development* **144,** 552–566 CrossRef Medline
3. Heisenberg, C. P., and Bellaïche, Y. (2013) Forces in tissue morphogenesis and patterning. *Cell* **153,** 948–962 CrossRef Medline
4. Lecuit, T., and Yap, A. S. (2015) E-cadherin junctions as active mechanical integrators in tissue dynamics. *Nat. Cell Biol.* **17,** 533–539 CrossRef Medline
5. Takeichi, M. (2014) Dynamic contacts: Rearranging adherens junctions to drive epithelial remodelling. *Nat. Rev. Mol. Cell Biol.* **15,** 397–410 CrossRef Medline
6. Martin, A. C., and Goldstein, B. (2014) Apical constriction: Themes and variations on a cellular mechanism driving morphogenesis. *Development* **141,** 1987–1998 CrossRef Medline
7. Arnold, T. R., Stephenson, R. E., and Miller, A. L. (2017) Rho GTPases and actomyosin: Partners in regulating epithelial cell-cell junction structure and function. *Exp. Cell Res.* **358,** 20–30 CrossRef Medline
8. Verma, S., Shewan, A. M., Scott, J. A., Helwani, F. M., den Elzen, N. R., Miki, H., Takenawa, T., and Yap, A. S. (2004) Arp2/3 activity is necessary for efficient formation of E-cadherin adhesive contacts. *J. Biol. Chem.* **279,** 34062–34070 CrossRef Medline
9. Kovacs, E. M., Goodwin, M., Ali, R. G., Paterson, A. D., and Yap, A. S. (2002) Cadherin-directed actin assembly: E-cadherin physically associates with the Arp2/3 complex to direct actin assembly in nascent adhesive contacts. *Curr. Biol.* **12,** 379–382 CrossRef Medline
10. Otani, T., Ichii, T., Aono, S., and Takeichi, M. (2006) Cdc42 GEF Tuba regulates the junctional configuration of simple epithelial cells. *J. Cell Biol.* **175,** 135–146 CrossRef Medline
11. Tang, V. W., and Brieher, W. M. (2012) α-Actinin-4/FSGS1 is required for Arp2/3-dependent actin assembly at the adherens junction. *J. Cell Biol.* **196,** 115–130 CrossRef Medline
12. Verma, S., Han, S. P., Michael, M., Gomez, G. A., Yang, Z., Teasdale, R. D., Ratheesh, A., Kovacs, E. M., Ali, R. G., and Yap, A. S. (2012) A WAVE2-Arp2/3 actin nucleator apparatus supports junctional tension at the epithelial zonula adherens. *Mol. Biol. Cell* **23,** 4601–4610 CrossRef Medline
13. Campellone, K. G., and Welch, M. D. (2010) A nucleator arms race: cellular control of actin assembly. *Nat. Rev. Mol. Cell Biol.* **11,** 237–251 CrossRef Medline
14. Goode, B. L., and Eck, M. J. (2007) Mechanism and function of formins in the control of actin assembly. *Annu. Rev. Biochem.* **76,** 593–627 CrossRef Medline
15. Skau, C. T., and Waterman, C. M. (2015) Specification of architecture and function of actin structures by actin nucleation factors. *Annu. Rev. Biophys.* **44,** 285–310 CrossRef Medline
16. Kühn, S., and Geyer, M. (2014) Formins as effector proteins of Rho GTPases. *Small GTPases* **5,** e983876 CrossRef Medline
17. Grikscheit, K., and Grosse, R. (2016) Formins at the junction. *Trends Biochem. Sci.* **41,** 148–159 CrossRef Medline
18. Homem, C. C., and Peifer, M. (2008) Diaphanous regulates myosin and adherens junctions to control cell contractility and protrusive behavior during morphogenesis. *Development* **135,** 1005–1018 CrossRef Medline
19. Massarwa, R., Schejter, E. D., and Shilo, B. Z. (2009) Apical SEcretion in epithelial tubes of the *Drosophila* embryo is directed by the formin-family protein Diaphanous. *Dev. Cell* **16,** 877–888 CrossRef Medline
20. Phng, L. K., Gebala, V., Bentley, K., Philippides, A., Wacker, A., Mathivet, T., Sauteur, L., Stanchi, F., Belting, H. G., Affolter, M., and Gerhardt, H. (2015) Formin-mediated actin polymerization at endothelial junctions is required for vessel lumen formation and stabilization. *Dev. Cell* **32,** 123–132 CrossRef Medline
21. Kobielak, A., Pasolli, H. A., and Fuchs, E. (2004) Mammalian formin-1 participates in adherens junctions and polymerization of linear actin cables. *Nat. Cell Biol.* **6,** 21–30 CrossRef Medline
22. Carramusa, L., Ballestrem, C., Zilberman, Y., and Bershadsky, A. D. (2007) Mammalian diaphanous-related formin Dia1 controls the organization of E-cadherin-mediated cell-cell junctions. *J. Cell Sci.* **120,** 3870–3882 CrossRef Medline
23. Grikscheit, K., Frank, T., Wang, Y., and Grosse, R. (2015) Junctional actin assembly is mediated by formin-like 2 downstream of Rac1. *J. Cell Biol.* **209,** 367–376 CrossRef Medline
24. Nishimura, T., Ito, S., Saito, H., Hiver, S., Shigetomi, K., Ikenouchi, J., and Takeichi, M. (2016) DAAM1 stabilizes epithelial junctions by restraining WAVE complex-dependent lateral membrane motility. *J. Cell Biol.* **215,** 559–573 CrossRef Medline
25. Acharya, B. R., Wu, S. K., Lieu, Z. Z., Parton, R. G., Grill, S. W., Bershadsky, A. D., Gomez, G. A., and Yap, A. S. (2017) Mammalian Diaphanous 1 mediates a pathway for E-cadherin to stabilize epithelial barriers through junctional contractility. *Cell Rep.* **18,** 2854–2867 CrossRef Medline
26. Kan-O, M., Takeya, R., Abe, T., Kitajima, N., Nishida, M., Tominaga, R., Kurose, H., and Sumimoto, H. (2012) Mammalian formin Fhod3 plays an essential role in cardiogenesis by organizing myofibrillogenesis. *Biol. Open.* **1,** 889–896 CrossRef Medline
27. Massarwa, R., and Niswander, L. (2013) *In toto* live imaging of mouse morphogenesis and new insights into neural tube closure. *Development* **140,** 226–236 CrossRef Medline
28. Wilson, D. B., and Wyatt, D. P. (1995) Patterns of lectin binding during mammalian neurogenesis. *J. Anat.* **186,** 209–216 Medline
29. Morriss-Kay, G., and Tuckett, F. (1985) The role of microfilaments in cranial neurulation in rat embryos: Effects of short-term exposure to cytochalasin D. *J. Embryol. Exp. Morphol.* **88,** 333–348 Medline
30. Hildebrand, J. D., and Soriano, P. (1999) Shroom, a PDZ domain-containing actin-binding protein, is required for neural tube morphogenesis in mice. *Cell.* **99,** 485–497 CrossRef Medline
31. Ohmura, T., Shioi, G., Hirano, M., and Aizawa, S. (2012) Neural tube defects by NUAK1 and NUAK2 double mutation. *Dev. Dyn.* **241,** 1350–1364 CrossRef Medline
32. Grego-Bessa, J., Hildebrand, J., and Anderson, K. V. (2015) Morphogenesis of the mouse neural plate depends on distinct roles of cofilin 1 in apical and basal epithelial domains. *Development* **142,** 1305–1314 CrossRef Medline
33. Suzuki, M., Morita, H., and Ueno, N. (2012) Molecular mechanisms of cell shape changes that contribute to vertebrate neural tube closure. *Dev. Growth Differ.* **54,** 266–276 CrossRef Medline
34. Sawyer, J. M., Harrell, J. R., Shemer, G., Sullivan-Brown, J., Roh-Johnson, M., and Goldstein, B. (2010) Apical constriction: A cell shape change that can drive morphogenesis. *Dev. Biol.* **341,** 5–19 CrossRef Medline
35. Lee, H. O., and Norden, C. (2013) Mechanisms controlling arrangements and movements of nuclei in pseudostratified epithelia. *Trends Cell Biol.* **23,** 141–150 CrossRef Medline
36. Yonemura, S., Wada, Y., Watanabe, T., Nagafuchi, A., and Shibata, M. (2010) α-Catenin as a tension transducer that induces adherens junction development. *Nat. Cell Biol.* **12,** 533–542 CrossRef Medline
37. Ybot-Gonzalez, P., and Copp, A. J. (1999) Bending of the neural plate during mouse spinal neurulation is independent of actin microfilaments. *Dev. Dyn.* **215,** 273–283 CrossRef Medline
38. Hirano, S., and Takeichi, M. (2012) Cadherins in brain morphogenesis and wiring. *Physiol. Rev.* **92,** 597–634 CrossRef Medline
39. Nishimura, T., Honda, H., and Takeichi, M. (2012) Planar cell polarity links axes of spatial dynamics in neural-tube closure. *Cell* **149,** 1084–1097 CrossRef Medline
40. Guthrie, S., Butcher, M., and Lumsden, A. (1991) Patterns of cell division and interkinetic nuclear migration in the chick embryo hindbrain. *J. Neurobiol.* **22,** 742–754 CrossRef Medline
41. Filas, B. A., Oltean, A., Majidi, S., Bayly, P. V., Beebe, D. C., and Taber, L. A. (2012) Regional differences in actomyosin contraction shape the primary vesicles in the embryonic chicken brain. *Phys. Biol.* **9,** 066007 CrossRef Medline
42. Shum, A. S., and Copp, A. J. (1996) Regional differences in morphogenesis of the neuroepithelium suggest multiple mechanisms of spinal neurulation in the mouse. *Anat. Embryol.* (*Berl.*) **194,** 65–73 Medline

43. Morriss-Kay, G. M. (1981) Growth and development of pattern in the cranial neural epithelium of rat embryos during neurulation. *J. Embryol. Exp. Morphol.* **65,** (suppl.) 225–241 Medline
44. Kida, Y., Shiraishi, T., and Ogura, T. (2004) Identification of chick and mouse *Daam1* and *Daam2* genes and their expression patterns in the central nervous system. *Dev. Brain Res.* **153,** 143–150 CrossRef Medline
45. Li, D., Hallett, M. A., Zhu, W., Rubart, M., Liu, Y., Yang, Z., Chen, H., Haneline, L. S., Chan, R. J., Schwartz, R. J., Field, L. J., Atkinson, S. J., and Shou, W. (2011) Dishevelled-associated activator of morphogenesis 1 (Daam1) is required for heart morphogenesis. *Development* **138,** 303–315 CrossRef Medline
46. Higashi, T., Stephenson, R. E., and Miller, A. L. (2018) Comprehensive analysis of formin localization in *Xenopus* epithelial cells. *Mol. Biol. Cell* **30,** 82–95 CrossRef Medline
47. Wu, S. K., Gomez, G. A., Michael, M., Verma, S., Cox, H. L., Lefevre, J. G., Parton, R. G., Hamilton, N. A., Neufeld, Z., and Yap, A. S. (2014) Cortical F-actin stabilization generates apical-lateral patterns of junctional contractility that integrate cells into epithelia. *Nat. Cell Biol.* **16,** 167–178 CrossRef Medline
48. Vaage, S. (1969) The segmentation of the primitive neural tube in chick embryos (*Gallus domesticus*): A morphological, histochemical and autoradiographical investigation. *Ergeb. Anat. Entwicklungsgesch.* **41,** 3–87 Medline
49. Kiecker, C., and Lumsden, A. (2005) Compartments and their boundaries in vertebrate brain development. *Nat. Rev. Neurosci.* **6,** 553–564 CrossRef Medline
50. Krumlauf, R. (2016) Hox genes and the hindbrain. *Curr. Top. Dev. Biol.* **116,** 581–596 CrossRef Medline
51. Dahmann, C., Oates, A. C., and Brand, M. (2011) Boundary formation and maintenance in tissue development. *Nat. Rev. Genet.* **12,** 43–55 CrossRef Medline
52. Calzolari, S., Terriente, J., and Pujades, C. (2014) Cell segregation in the vertebrate hindbrain relies on actomyosin cables located at the interhombomeric boundaries. *EMBO J.* **33,** 686–701 CrossRef Medline
53. Marín, F., Aroca, P., and Puelles, L. (2008) Hox gene colinear expression in the avian medulla oblongata is correlated with pseudorhombomeric domains. *Dev. Biol.* **323,** 230–247 CrossRef Medline
54. Gunning, P. W., Hardeman, E. C., Lappalainen, P., and Mulvihill, D. P. (2015) Tropomyosin: Master regulator of actin filament function in the cytoskeleton. *J. Cell Sci.* **128,** 2965–2974 CrossRef Medline
55. Nicholson-Flynn, K., Hitchcock-DeGregori, S. E., and Levitt, P. (1996) Restricted expression of the actin-regulatory protein, tropomyosin, defines distinct boundaries, evaginating neuroepithelium, and choroid plexus forerunners during early CNS development. *J. Neurosci.* **16,** 6853–6863 CrossRef Medline
56. Williams, M., Yen, W., Lu, X., and Sutherland, A. (2014) Distinct apical and basolateral mechanisms drive planar cell polarity-dependent convergent extension of the mouse neural plate. *Dev. Cell* **29,** 34–46 CrossRef Medline
57. Ushijima, T., Fujimoto, N., Matsuyama, S., Kan-o, M., Kiyonari, H., Shioi, G., Kage, Y., Yamasaki, S., Takeya, R., and Sumimoto, H. (2018) The actin-organizing formin protein Fhod3 is required for postnatal development and functional maintenance of the adult heart in mice. *J. Biol. Chem.* **293,** 148–162 CrossRef Medline
58. Sandell, L. L., Kurosaka, H., and Trainor, P. A. (2012) Whole mount nuclear fluorescent imaging: Convenient documentation of embryo morphology. *Genesis* **50,** 844–850 CrossRef Medline
59. Kanaya, H., Takeya, R., Takeuchi, K., Watanabe, N., Jing, N., and Sumimoto, H. (2005) Fhos2, a novel formin-related actin-organizing protein, probably associates with the nestin intermediate filament. *Genes Cells* **10,** 665–678 CrossRef Medline
60. Schindelin, J., Arganda-Carreras, I., Frise, E., Kaynig, V., Longair, M., Pietzsch, T., Preibisch, S., Rueden, C., Saalfeld, S., Schmid, B., Tinevez, J. Y., White, D. J., Hartenstein, V., Eliceiri, K., Tomancak, P., and Cardona, A. (2012) Fiji: An open-source platform for biological-image analysis. *Nat. Methods.* **9,** 676–682 CrossRef Medline
61. Matsuyama, S., Kage, Y., Fujimoto, N., Ushijima, T., Tsuruda, T., Kitamura, K., Shiose, A., Asada, Y., Sumimoto, H., and Takeya, R. (2018) Interaction between cardiac myosin-binding protein C and formin Fhod3. *Proc. Natl. Acad. Sci. U.S.A.* **115,** E4386–E4395 CrossRef Medline